Toward Simple Dynamic Metasurface Antennas for Reconfigurable Beamforming and AoA Detection

by

Travis Williams

A Thesis Presented in Partial Fulfillment
of the Requirements for the Degree
Masters of Science

Approved April 2024 by the
Graduate Supervisory Committee:

Seyedmohammadreza Faghih Imani, Chair
James Aberle
Georgios Trichopoulos

ARIZONA STATE UNIVERSITY

May 2024

ABSTRACT

Dynamic metasurface antennas (DMAs) consist of waveguides patterned with numerous metamaterial radiators loaded with switchable components (such as varactors). By applying different direct current (DC) signals to each element, DMAs can generate a multitude of radiation patterns ranging from directive beams useful for wireless communication to spatially diverse ones useful for computational imaging and sensing. In this thesis, DMAs are extended to conformal configurations. Using full-wave simulation, it is shown that a conformal DMA can detect the angle of the incident signal over the horizon using a two port device at a single frequency. The design and operation of the conformal DMA will be detailed. In addition, it shows that DMAs can be implemented using a single substrate layer, significantly simplifying its structure compared to conventional multiple-layer ones. Using full-wave simulation, this thesis demonstrates a mechanism to bring DC signal to metamaterial elements without requiring an extra layer. This design can be instrumental in implementing the conformal DMA in the future

AoA detection was achieved over unique diode distributions of the conformal DCMA at a 10-degree resolution. Investigations into additive noise of the simulated measured data as well as the minimum amount of diode distributions to accurately detect AoA were conducted and documented within this thesis. The single-layer DMA yielded both directive and complex patterns that allow for many potential applications. With success in bringing the DC signal to the metamaterial elements on a single-layer, further advances in conformal DMAs can be achieved.

ACKNOWLEDGMENTS

I would like to thank Dr. Imani for mentoring me throughout the work displayed in this thesis. Without his expertise and accommodations, the work presented could not have been completed. In conjunction, he was an excellent professor for both antenna courses I have taken with him making many of these topics more easily understandable. I would also like to acknowledge and thank my wonderful fiancée Sarah. Without her, this master's degree would not be possible without all the love and support you have supplied me over the past two years.

TABLE OF CONTENTS

CHAPTER Page

LIST OF FIGURES

Figure Page

Chapter 1

INTRODUCTION TO DYNAMIC METASURFACE ANTENNAS

1.1 Dynamic Metasurface Antennas

1.1.1 Metasurface Antennas

Metamaterials and metasurfaces utilize electrically small resonant scatterers, producing aggregate effects that are not readily available[1]. In particular, their ability to manipulate electromagnetic waves can be used to improve antenna radiation properties[2][3]. For example, metamaterials have been used to minimize antennas[4]. Metasurfaces are the two-dimensional counterpart of the three-dimensional metamaterials and will be the building block of the work in this thesis. Their two-dimensional attribute leads to physically smaller devices and the potential for lower losses compared to the three-dimensional counterpart [5]. Metasurface antennas of different shapes and functionalities have been proposed over the last decade and have found a wide range of applications, from computational imaging for security screening purposes to wireless communication systems[6][7][8].

1.1.2 Frequency Diverse Metasurface Antennas

One unique implementation of metasurface antennas that has revolutionized microwave imaging is to etch metamaterial elements designed to exhibit distinct resonant frequencies onto a microstrip transmission line [9]. These elements are randomly distributed along the microstrip line. In this manner, as the waveguide mode travels along the microstrip, it will weakly couple to a number of the resonant metamaterial elements with resonance frequencies near the guided mode's frequency. As the frequency of the guided mode changes, different sets of elements get excited, resulting in spatially diverse radiation patterns that

change as a function of frequency, hence the name *frequency-diverse* metasurface. These frequency-diverse radiation patterns can encode the spatial distribution of an imaging scene into frequency measurements. The measurements collected in this manner can be computationally processed to form an image of the scene's reflectivity map. This idea was experimentally demonstrated in [9]. In this configuration, the metasurface antenna replaced a large phased or switch array with a simple configuration, eliminating the need for many complex and costly components. Since this work, frequency-diverse metasurfaces have found many other applications, such as angle of arrival (AoA) detection (see for example [10][11][12][13]).

1.1.3 Dynamic Metasurface Antennas

Dynamic metasurface antennas (DMAs) are constructed by turning the building blocks of the aforementioned frequency-diverse metasurface elements into reconfigurable ones by loading them with tunable components such as positive-intrinsic-negative (PIN) or varactor diodes. PIN diodes in reverse bias can turn *on* a metamaterial element and allow it to radiate while elements loaded with forward-biased PIN diodes will be approximately electrically shorted, leading to no contribution to the radiated pattern [6][7][14]. Varactor diodes, on the other hand, can be biased with different voltages to shift resonances more continuously, providing more control over the amplitude and phase of the radiated signal[15]. Regardless of the type of tunable component, reconfigurable elements of DMAs need to be addressed independently, necessitating a DC biasing circuitry. Typically, this circuitry is implemented on another layer, which increases the complexity and cost of the DMA. However, their ability to generate spatially diverse patterns as a function of electronic signal essentially allows a DMA to replace a large array of antennas, justifying the more complicated structure. DMAs also do not require frequency bandwidth, which further simplifies the overall structure[16]. Imaging systems utilizing DMAs can assist in critical areas such as security

screenings and through-wall imaging [6][7][14].

1.2 Planar vs Conformal Metasurface Antennas

The majority of previous studies on metasurfaces have been on planar rigid configurations (i.e., non-conformal). In many applications, it is desired due to mechanical or stealth constraints that the antenna structure conforms to the object surface. Conformal metasurface antennas (CMAs), which can take the shape of structures, have seen less exposure than that of planar ones. The rigid structure of non-conformal antennas makes it challenging to integrate them into the curved surface of most objects (such as vehicles, airplanes, missiles, helmets, etc.). Furthermore, conformal structures are better suited for certain applications. For example, realizing a 360-degree field of view for imaging or sensing using planar structures is not straightforward. A conformal metasurface can provide the desired field of view while also providing the benefits of metasurface antennas in terms of simplicity and cost-effectiveness. An option with more potential is dynamic Conformal Metasurface Antennas (DCMAs) that can conform to any arbitrarily shaped surface and deliver similar performance (as well as advantages) as non-conformal DMAs.

1.3 Contributions

In this thesis, we first examine the feasibility of angle of arrival detection using DCMA. Using full-wave simulation, we show that a DCMA can detect incident angles from any direction over the horizon (i.e., full 360 degrees) from a simple two-port device that operates at a single frequency. We then work on addressing some practical challenges in implementing the desired DCMA. While DCMAs and DMAs consume less power and are less expensive than conventional phased arrays or switch arrays, the need for multiple layers rather than a single substrate and radiating layer increases the cost and complexity of manufacturing. Implementing a conformal multilayer structure is also more complicated. As

a result, designing a DMA to have DC bias circuitry on the same layer as radiating elements allows DMAs to have an overall simpler configuration, lighter weight, and more straightforward fabrication process, especially for a DCMA.

Chapter 2

CONFORMAL DYNAMIC METASURFACE FOR SENSING

2.1 Review of Previous Work on Conformal Metasurface Antennas

The interest in CMAs for imaging and sensing has grown over the last few years. This interest stems from the fact that the conformal low profile nature of CMAs makes them ideal for a wide array of applications ranging from angle of arrival (AoA) detection [8], brain tumor detection [17], beamforming[18][19], microwave imaging[8][19], radar cross-section reduction (RCSR) [20][21], among others. In all of these applications, many antenna elements need to conform to an arbitrary shape, a property that can be easily realized by applying metasurface antenna design concepts. Having a conformal profile allows the antenna to be ideal for military applications where low radar cross-section (RCS) is desired or when mechanical and aerodynamic constraints are the limiting factor, e.g., in aircraft and missiles.

Circular polarization generation is a particular area where CMAs can benefit wireless communications [22]. In [23] a conformal anisotropic holographic metasurface was designed to transform traveling surface waves at discontinuities of the elements from a linear polarized to circularly polarized wave with high conversion efficiency. [22] took a different approach to printing the antenna on conformal PET. The original feed patch antenna was able to generate circularly polarized beams without, the metasurface elements but, the metasurface elements are designed to improve the axial ratio and circularly polarized operating bandwidth.

The ability to form and steer a beam is an attractive attribute of any antenna or array. However, beamforming from conformal surfaces is more challenging due to requirements

set by the surface shape. In these cases, typical phased arrays may not yield the desired performance due to phase ambiguity, cost, and overall complexity. These issues can be overcome by CMAs, which can more easily accommodate different surface shapes. Earlier work on this topic for CMAs includes [18] which utilized metamaterial-based leaky-wave transmission line antennas. This structure could support both guided and radiated waves depending on the loading of the metamaterial elements. Varactor diodes were used to vary capacitance loading the DCMA elements, thus allowing it to switch between guided or radiated wave mode. This capability enabled control of beam width and an improved ability in steering. Alternatively, [19] used a conformal waveguide-fed metasurface antenna. Waveguide-fed metasurface antennas have been gaining popularity due to their low profile, low cost, and flexibility in beamforming. Using a dielectric-filled waveguide with resonant cELC resonator elements etched into the top walls [19] was able to achieve pattern synthesis by both simulation and analytical modeling.

2.2 Computational Sensing using Conformal Metasurface Antennas using Frequency Diversity

In this section, we review the work in [8], which will form the basis for the work in the Thesis. In [8] a frequency-diverse CMA was designed for AoA detection. In this work, the upper conductor of a conformal substrate integrated waveguide (SIW) was fashioned with multiple etched I-shaped metamaterial resonators slot antennas with varying geometries. The distinct geometry of each I-shape slot resulted in elements with diverse resonance frequencies. Geometries of the I-shape elements were randomly assigned to ensure the resonance frequencies would expand over the intended operating bandwidth. As a result, only a subset of elements with resonance frequency near the frequency of the guided wave would radiate, creating angularly diverse radiation patterns as a function of frequency. These frequency dependent radiation patterns had the ability to encode information about

the incident signal into simple frequency sweeps. Two simple coaxial feeds were used to collect the signal. The correlation between the voltage measurements at the end of the coaxial cables was used as the basis for detecting the incident AoA through computational analysis. The proposed design could multiplex information about the incident signal in the horizontal or azimuthal direction with full coverage of 0 to 360 degrees. This approach allowed for replacing a large conformal antenna array or a mechanically rotating antenna, which are typically used for AoA detection, with a simple two-port device.

Having elements resonant at different frequencies requires a relatively large operational bandwidth to achieve the desired performance. This is an inherent problem of frequency-diverse systems[24]. My work in this thesis is to examine whether reconfigurable metamaterial resonators could provide a similar performance but at a single frequency, significantly reducing the needed bandwidth. Furthermore, the frequency-diverse method could only detect a single AoA, which can limit its utility in some applications.

2.3 Design of Reconfigurable Metamaterial Elements for Conformal Structures

To investigate the feasibility of AoA detection using a DCMA, we need to first design the building block of the DCMA: a reconfigurable metamaterial element. For the feasibility study, we start with the same I-shape geometry as in the frequency-diverse conformal metasurface. We then introduce a diode across the I-shape gap. Diodes for each element design are simulated as lumped RLC components using Ansys HFSS. When including the PIN diodes, we need to ensure the effective capacitance is selected such that the resonance of the element is within the desired operating bandwidth of 9.5-10.5 GHz. The geometry of the metamaterial resonators will also act as a design knob to tune the resonant frequency.

The geometry of the I-shaped element is shown in Figure 2.1. This metamaterial element is the same as the one used in [8] but with a PIN diode added to create a reconfigurable metamaterial element. In contrast to the frequency diverse one which used el-

ements with different geometries, the geometrical parameters such as height, *h*, and width, *w*, shown labeled in Figure 2.1 will be the same for all the elements (i.e. one single resonance frequency) in contrast to the one in [8] which used different geometries to produce different resonance frequencies. The I-shape gap is 1.5 mm to allow room for the PIN diode

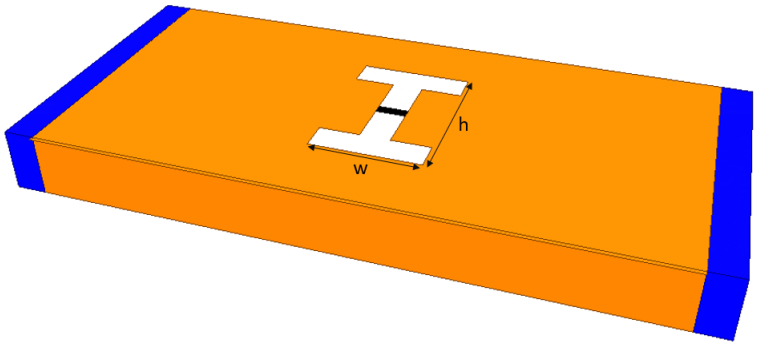

Figure 2.1: Metamaterial - Geometrical Structure

that is centered on the element. As previously mentioned PIN diodes used in reversed bias allow for the metamaterial element to radiate the guided wave of the SIW, while the forward bias will effectively result in an electrical short preventing radiation from the element. The ability to turn on/off an element will be very important for this design. Using the capacitance value of the lumped RLC in HFSS as a variable for the parametric sweep, a simulation of the setup in Figure 2.1 was conducted to find various resonances based on capacitance value and the *h*, *w*, and as well the gap size.

With the final design of this element having a *h* = 8 mm, *w* = 5.5 mm, reverse biased resistance R_{rev} = 10 kΩ, and reverse biased capacitance C_{rev} = 1.75 pF. Forward-biased resistance resulted in a value of R_{fwd} = 2 Ω and the forward-biased capacitance of C_{fwd} = 0 pF. Figure 2.3 and Figure 2.2 show the S_{21} and S_{11} respectively for the forward and reversed biased configuration. It is clear that when the element is in an "off" state or the diode is forward biased, most of the signal passes through without radiation (thus high S_{21}).

On the other hand, when the element is ”on,” and the diode is reverse biased, the element couples to the SIW-guided mode and radiates. As can be seen, it is expected that the largest amount of radiation happens at around 9.5 GHz. However, when we use elements next to each other in the SIW geometry, the resonance frequency of each element may shift due to the parasitic loading of additional elements on the structure. Furthermore, given the high level of coupling, operating at off-resonance may be beneficial since at resonance, a large portion of the signal radiates without reaching the subsequent elements. These factors will be studied in more detail to follow.

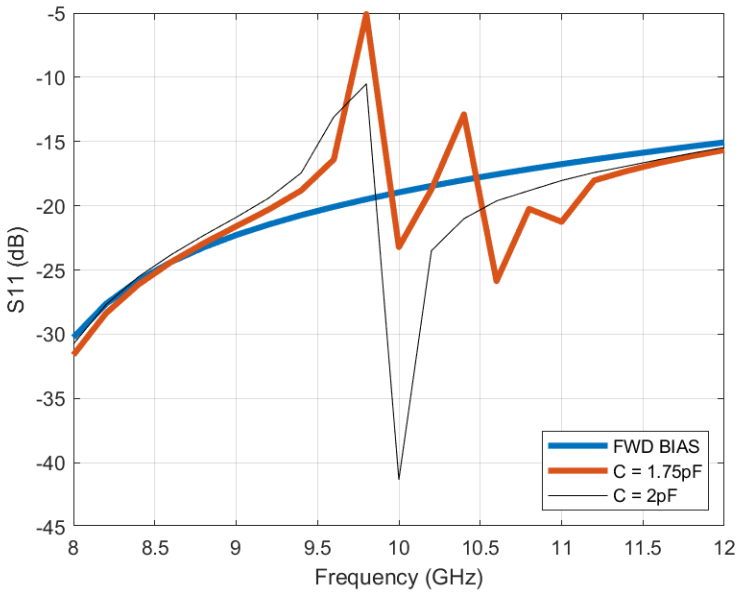

Figure 2.2: S11(dB) - Comparison of Reversed and Forward Bias

2.4 General Configuration of Dynamic Conformal Metasurface

2.4.1 General Design of Dynamic Conformal Metasurface

The proposed DCMA consists of a conformal SIW antenna with 34 elements etched onto its top layer at 10-degree increments as shown in Figure 2.4. This SIW is connected to two coaxial connectors at the two opposite edges. We first analyze this structure's recep-

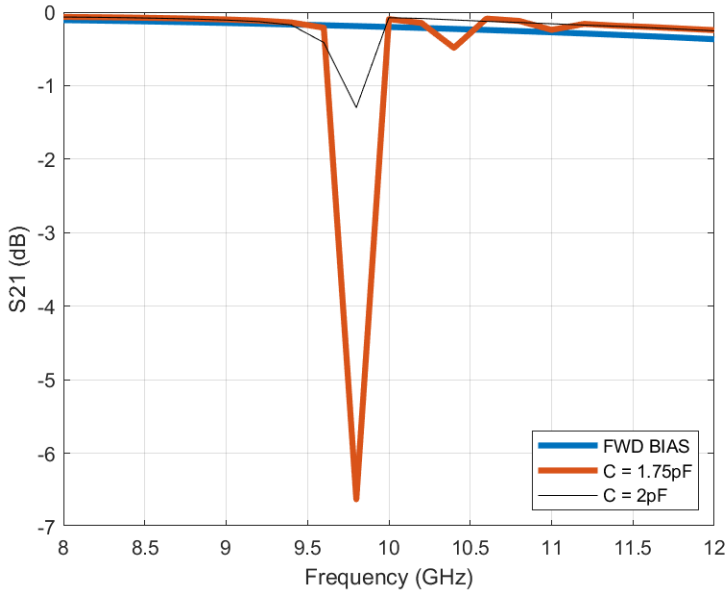

Figure 2.3: S21(dB) - Comparison of Reversed and Forward Bias

tion/radiation patterns as we change the distribution of on and off elements. For brevity, we will refer to the ”on” and ”off” arrangements of diodes as a mask. The results of this simulation for a collection of masks are shown in Figure 2.7. It is important to note that there are 34 elements, which in total can result in 2^{34} masks. In practice, we do not expect to obtain more than 34 independent measurements. So, it is sufficient to examine only ≈ 34 masks. To do that and to simplify the simulation setup, we grouped the 34 elements into random groups of 6-7 elements. The breakdown of the groupings consists of one grouping of 6 and four groupings of 7 elements for 5 total distinct options to turn on or off elements. With this approach, there are 32 potential unique voltage masks rather than a number in the billions (i.e. 2^{34}). Limiting to these groups not only greatly reduces the large amount of time for simulation but, also eliminates potential weak voltage masks from single elements on opposing sides of the cylindrical DCMA. The 32 voltage masks include the all-on and all-off cases that will only be examined to compare with other cases. Similar to that of [8] PEC walls were used in place of the SIW vias for ease of simulation and reduction of

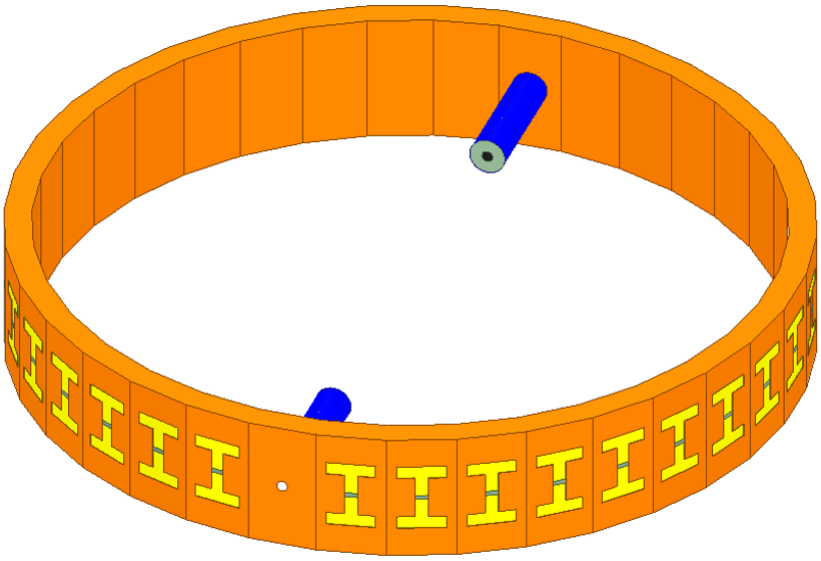

Figure 2.4: DCMA Design

complexity. The structure was also confined within PMC walls to emulate a 2D geometry to further reduce simulation complexity.

2.4.2 Complex Pattern Generation of 'Etched I-Shape Resonator'

Evaluating the potential patterns of the first elements design was carried out including all 32 potential voltage masks. This includes both the all-on and all-off masks. Originally, the larger resonance shown in Figure 2.3 was attempted, yielding no variation in the pattern reflecting a resonance shift. Adjustments were made based on the S21 of the antenna resulting in the resonance of 10.4 GHz. During simulation, a frequency sweep was conducted at +/- 100 MHz from the resonant frequency of 10.4 GHz to evaluate whether a strong maximum radiated envelope tracked over a larger bandwidth. The maximum radiated envelope is the thick black line showing the maximum of all masks over angle ϕ of the normalized directivity cut of ϕ. Ideally, the pattern maximum envelope would be near a flat line at the maximum boundary of 0 dB for equivalent coverage at all angles. Starting with the direc-

tivity of 10.5 GHz shown in Figure 2.5 which had the least desirable coverage and strength of the signal in directions of ϕ. Next, reviewing the other frequency extreme at 10.3 GHz

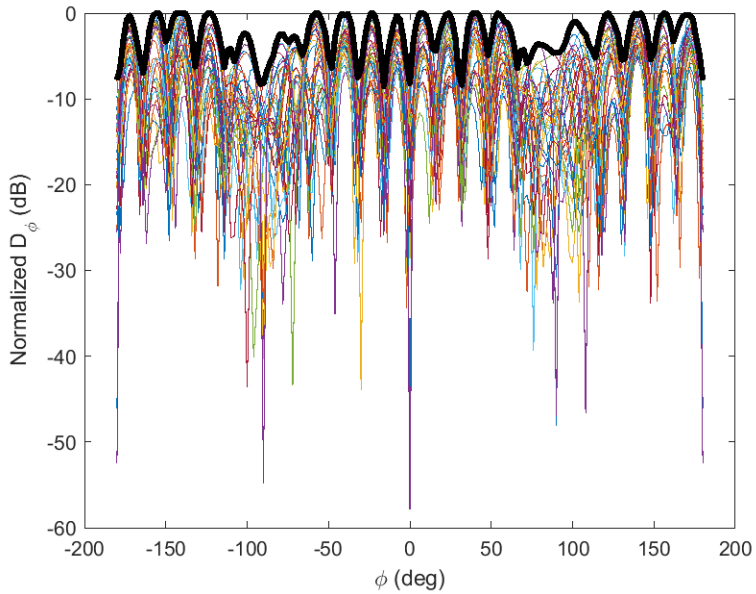

Figure 2.5: Normalized D_ϕ at 10.5 GHz of All Voltage Masks

of this study yields slightly better coverage than that of 10.5 GHz as shown in Figure 2.6. There are fewer angles where the envelope is not reflected as a maximum. Pointing towards more variation in this frequency as a result of the re-configurable resonance of the DCMA. Finally, inspecting the resonant frequency of the DCMA displays great coverage amongst the 32 voltage masks. Results are shown in Figure 2.7, where the maximum coverage of the radiated envelope yields highly improved signal strength between 50-100 degrees in comparison to the previous two frequency cases. The improvement in coverage is due to the effect of the PIN diode at the resonant frequency. Resulting in improved radiation from the whole surface of the DCMA.

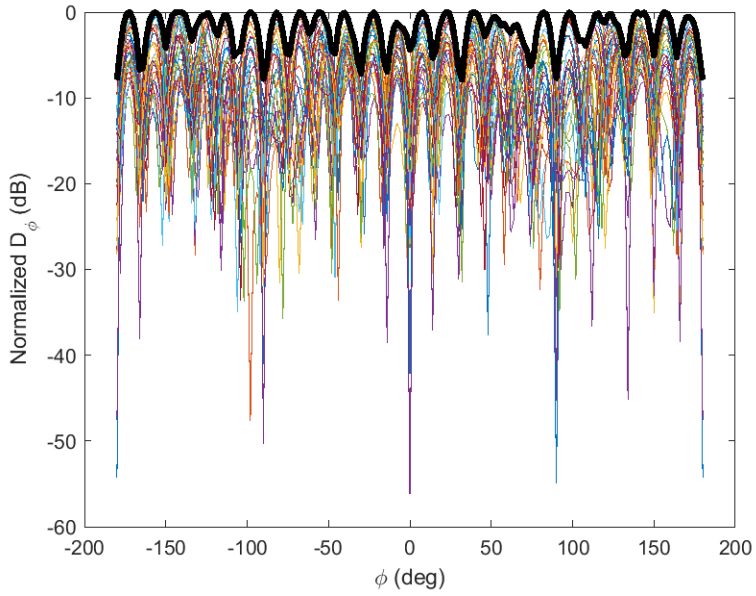

Figure 2.6: Normalized D_ϕ at 10.3 GHz of All Voltage Masks

2.4.3 AoA Sensing Protocol

Now that we ensure the proposed device can form multiplexing radiation patterns, we develop the sensing protocol. To do that, we use a similar computational sensing method as in [8]. The first step in this method is to form a sensing matrix that relates the measured signal to the incident angle of arrival for a set of reference angles. Sensing for AoA detection in this design is done by measuring the complex voltages at each simple coaxial feed. Much like the spacing of 10-degree increments used for the etched elements, incident waves impinging on the structure will be excited at 10-degree increments for a total coverage of 360 degrees. This gives 36 unique incident reference angles as well as a maximum of 30 voltage masks; excluding all on and off cases for the AoA detection study. Measurement of the complex voltages at the simple feeds is carried out by full-wave numerical simulations and the ports are denoted V_1 and V_2. Regardless of the number of voltage masks simulated in either design, a $M \times N$ reference matrix denoted $\mathbf{H}$ can be formed. *M* voltage masks and *N* reference angles build $\mathbf{H}$ where the *m*th voltage mask,f_m and the *n*th reference angle,ϕ_{ref}^n,

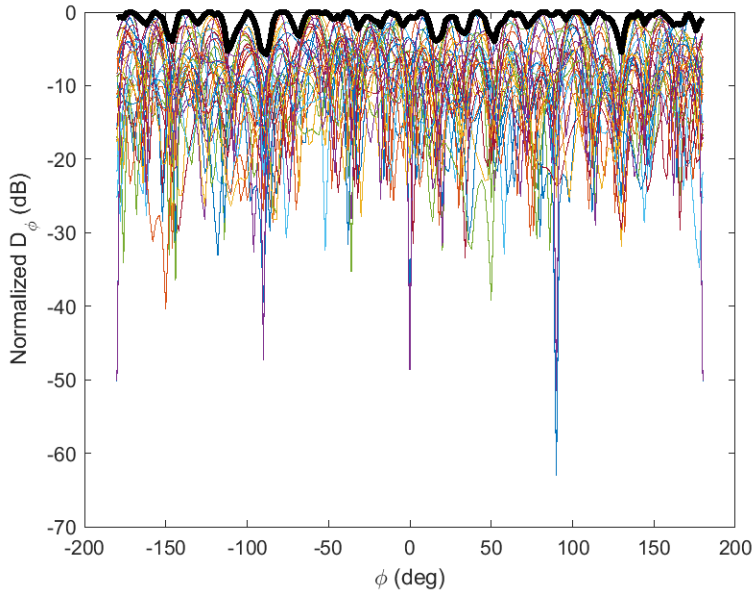

Figure 2.7: Normalized D_ϕ at 10.4 GHz of All Voltage Masks

are derived from (2.1).

$$h_{mn} = V_2 - V_1 \text{ for } f_m, \phi^n_{ref} \tag{2.1}$$

To first test AoA detection, we investigate the accuracy of reference angles that constructed $\mathbf{H}$ by deriving $\mathbf{g}$ from (2.2).

$$g_{Mx1} = \mathbf{H}_{MxN}\mathbf{f}_{Nx1} \tag{2.2}$$

In (2.2), $\mathbf{f_{Nx1}}$, is a vector with the *n*th element denoted as 1 to evaluate the associated reference angle and 0 otherwise. $\mathbf{g}$ can then be evaluated to estimate $\mathbf{f}$ using (2.2). This is similar to that of [8] however we are using voltage masks at a single frequency where the authors used multiple frequencies to construct the rows of $\mathbf{H}$ requiring a large bandwidth. As noted in [8] $\mathbf{H}$ is not a square matrix; resulting in an undefined inverse. Incident signals may also come from angles outside the reference set. Leading to the reliance on computational solvers. In this thesis, we will take advantage of the MATLAB conjugate gradients squared method (*cgs*) resulting in a vector $\mathbf{f_{est}}$ with a maximum peak at the nearest detected

AoA. Enabling the potential for AoA detection at angles outside the reference angles set of $\mathbf{H}$. In the Sensing Results section of this thesis, this procedure will be followed for both the reference angles as well as testing its ability to detect multiple angles included in the reference dataset. When constructing $\mathbf{g}$ random variations in amplitude and phase are added to ensure varying distance as well as phase ambiguity of the incident signal does not perturb the performance. In addition, a study on the signal-to-noise ratio (SNR) will be evaluated on the incident signal by adding built-in additive white Gaussian noise from a built-in function in MATLAB.

2.5 Sensing Results

All 30 potential voltage masks were simulated to examine sensing performance. Following the aforementioned sensing protocol of this chapter, we will first evaluate the diversity of the sensing matrix $\mathbf{H}$ which dictates AoA detection accuracy. Ideally, a smaller quantity of voltage masks could accurately estimate the AoA which, in turn, would require fewer measurements (faster data acquisition). Thus we evaluate different numbers of voltage masks of $\mathbf{H}$ through the use of the built-in MATLAB function for standard value decomposition (SVD). Results for the normalized SVD of $\mathbf{H}$ are shown in Figure 2.8. We can see that as we increase number of masks, the SVD indicates a larger set of diverse patterns. However, with 16 masks, there appears to be a slight separation, indicating a small improvement. The normalized SVD exhibits a diminishing return: a higher number of masks does not result in significantly larger diversity among measurements. In other words, the number of masks can be reduced without significantly impacting detection accuracy. It is important to note that as the sensing tasks becomes more complicated (e.g. detecting multiple AoAs or when noise is higher, larger number of masks would help). To test the sensing protocol, we examine cases where the test incident angle coincides with the reference angle but comes from a different distance (random amplitude and phase variation

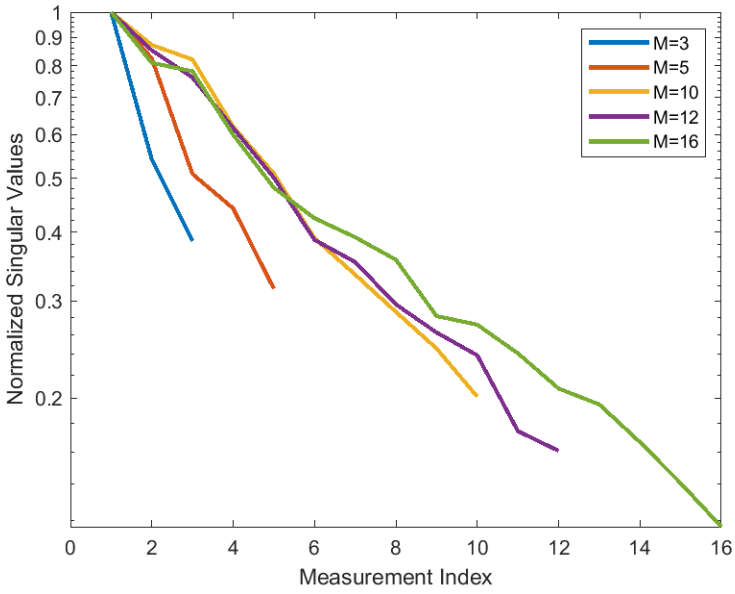

Figure 2.8: Normalized SVD of Different Subsets of Voltage Masks

from the reference angle). Accounting for SNR we evaluated the case of both 20 and 50 dB of noise through the MATLAB built-in function additive white Gaussian noise to g and reevaluated the results from the *cgs* solver. The results for the 16 voltage mask cases are included in Figure 2.9. With the additive noise, we were still able to detect all reference angles even when SNR reduces. To expand on this study we limited the voltage masks of $\mathbf{H}$ to 10 to examine accuracy with less data, correlating with fewer measurements. Results for the 10 voltage masks case are shown in Figure 2.10. For the reference and 50 dB SNR yielded all correctly detected. However, decrease in SNR slightly degrade the performance. Smaller sets of voltage masks were also tested and for the case of 8 or fewer voltage masks, the AoA detection using *cgs* quickly starts to degrade with erroneous results. As an example, results for 8 voltage masks are shown in Figure 2.11. In this case, even the reference without added white Gaussian noise incorrectly detects at two incident angles. Reductions from this case quickly led to over half the detected angles being incorrectly detected. The results track well with that of the SVD analysis for the varying quantities of voltage masks.

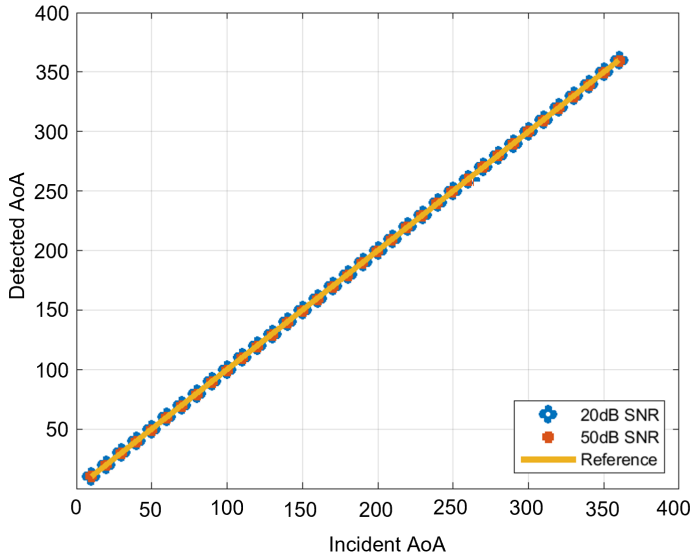

Figure 2.9: Detection of AoA of Reference Incident Angles of 16 Voltage Masks with SNR Evaulation

The smaller groupings are less accurate than that of the larger than 10 voltage masks that converge until the point of diminishing returns occurs in Figure 2.8, with smaller sets diverging from the grouping. The results for the 10 and above voltage masks constitute this design successful in AoA detection for the case of a single incident angle.

Further expanding on this study, we examined the plausibility of multiple incident angles being detected. Using the same technique to construct $\mathbf{g}$ in equation 2.2 a second $\mathbf{g}$ was formed with its own individual variance in amplitude and phase (a second source at a different distance and with a different phase). The two $\mathbf{g}$ terms are summed and examined through the *cgs* solver as before for the single angle study. With the expectation of multiple AoA the two highest peaks of $\mathbf{f}_{\mathbf{est}}$ are selected to correlate the two separate detected angles. With this approach, an accuracy of 73% was obtained for detecting both angles shown in Figure 2.12. This method however does produce an issue as seen in Figure 2.12 along the diagonal at which the two angles are equivalent. It is shown when one angle is +/- 10 degrees from the second angle of interest it may not be detected. This is a potential side effect of using the MATLAB function *findpeaks*. If the other angle of interest lies on

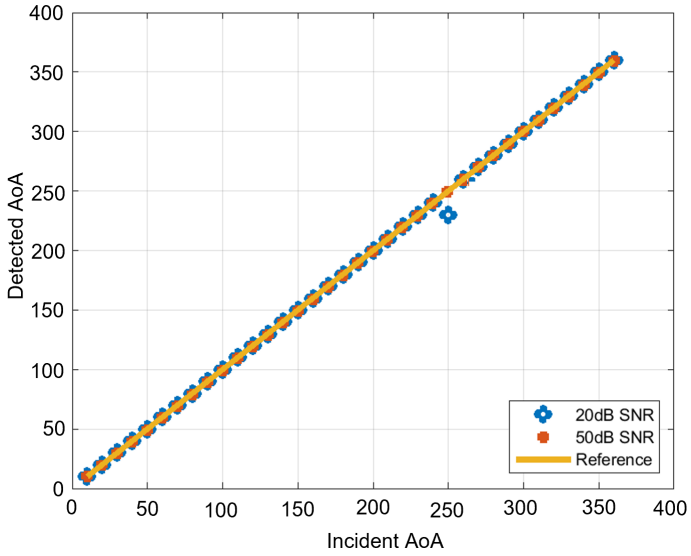

Figure 2.10: Detection of AoA of Reference Incident Angles of 10 Voltage Masks with SNR Evaulation

the downward curve of the maximum detected peak without producing its own peak it will not be detected. There are a few ways to counteract this; for example using the MATLAB function *maxk* to detect the two maximum values across reference angles eliminating the reliance on formed peaks.

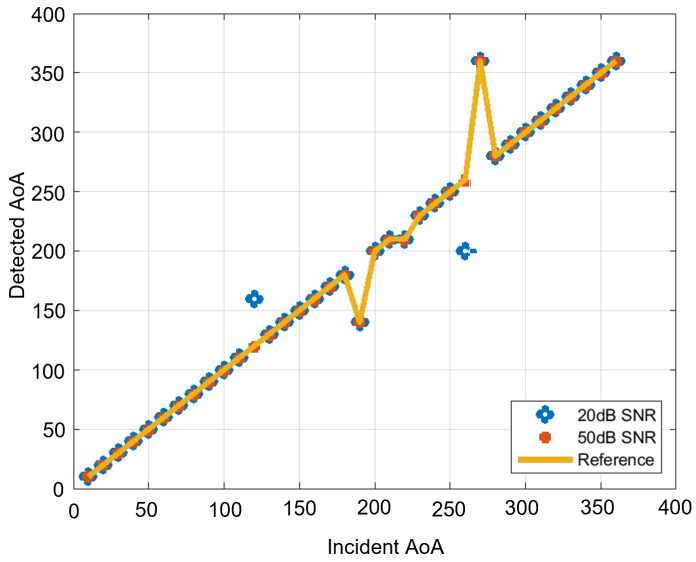

Figure 2.11: Detection of AoA of Reference Incident Angles of 8 Voltage Masks with SNR Evaulation

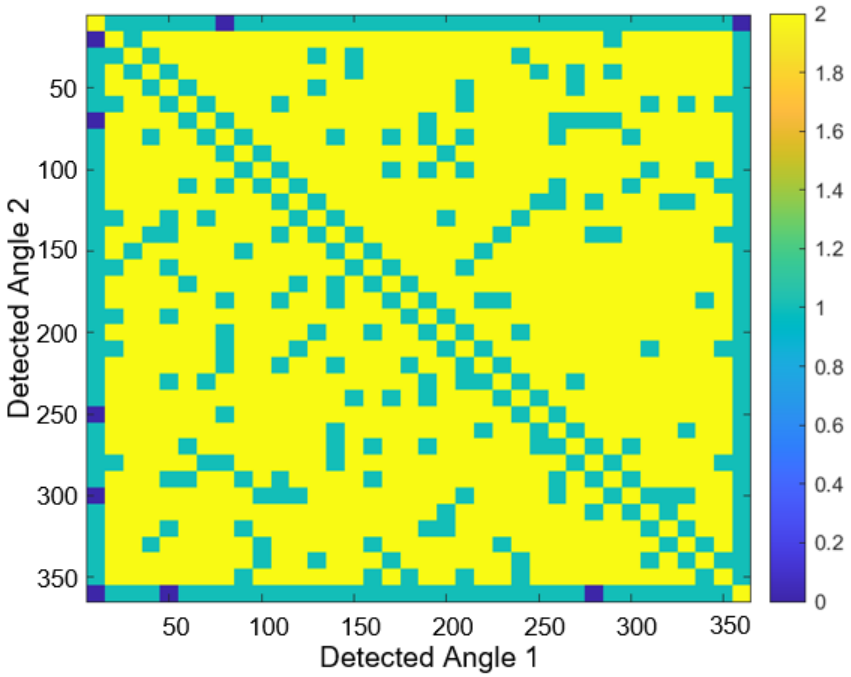

Figure 2.12: Study for Detection of Two AoA - Peaksearch Method

Chapter 3

SIMPLIFIED METAMATERIAL ELEMENT

3.1 Waveguide-fed Tunable Metamaterial Elements

Waveguide-fed tunable metamaterial elements have seen considerable exposure due to the ease of implementation, size, and costs. In these structures, metamaterial elements such as complimentary electric-LCs(cELCs) are patterned onto the conductive surfaces of waveguides[6][8][7][14][15][19]. These resonant subwavelength structures allow for coupling of the guided mode to the radiated fields. In [6] the design of a reconfigurable cELC resonator element excited by a microstrip line was detailed. This element was the building block of many DMAs developed later. This specific element will be the basis for the studies presented in this chapter.

The dynamic element designed in previous works required the introduction of a DC biasing circuitry. DC bias for metasurface antennas is nominally carried out on a different layer than the actual element. Vias are then introduced to carry the DC signal from the DC biasing layer to either an individual or multiple metamaterial elements. With the addition of each layer, the price and complexity of fabrication rise. Additional layers would also require bonding layers, alignment, and increased weight to the overall structure. Furthermore, conforming a multi-layer structure to arbitrary shapes is more challenging. To reduce the complexity and price of fabrication, it would be ideal to carry out the design of the DC and associated circuitry on the same layer as the metamaterial elements. This approach should come about with minimal degradation of the overall performance from the original design. A single-layer design will result in a thinner overall DMA. With fewer layers, the then-thinner DMA could more easily be constructed as a DCMA with varying bend radius

potentials.

Since this element will ultimately serve as the building block of an electrically large antenna, it will need to be weakly coupled to the guided wave. This ensures each element, no matter the distance from the feed, has sufficient power to couple from the guided wave, which enables reasonable radiation contributions. To enable reconfigurability, PIN diodes were introduced, allowing for the element either to be turned on or off. To carry this out vias were introduced and drilled through the ground layer to the bottom of the structure. A dielectric spacer was then implemented to keep the ground and DC biasing layer separated. It was important to prevent the RF signal coupling to the DC bias lines, which would reduce the antenna's overall performance. This led to the implementation of radial decoupling stubs on the DC bias layer, which mitigated coupling as desired. By turning on or off different combinations of the 8 elements resulted in various unique or directive radiation patterns making the design an ideal approach for communication systems, beamforming, or computational imaging applications. While the DMA achieves the desired performance for planar configurations, it would be very difficult to implement as a DCMA due to the added complexity of the extra layers. By bringing the DC bias and associated circuitry to the same layer as the radiating elements, a DCMA is more realizable.

3.2 Design of Single-layer Reconfigurable Element

The element configuration used in this chapter is based on that of [6]. A key difference however is the designed element is etched onto the surface of a substrate-integrated waveguide (SIW) rather than a microstrip line. To start the design the walls of the SIW were modeled as PEC rather than vias for ease of design as well as reduced time for the simulations carried out in Ansys HFSS. Initial designs were carried out with the metamaterial element centered on the structure with a width of 3.4 mm. The element at this state can be seen in Figure 3.1. As stated in [6] the labeled a and b in Figure 3.1 were varied

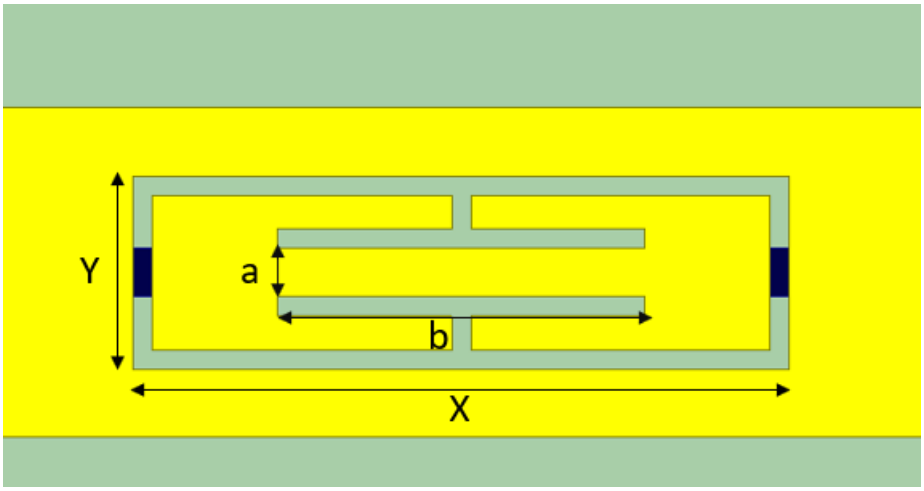

Figure 3.1: cELC Resonator Used in Design

to manipulate the inductance of the cELC resonator. The other geometrical constraints, X and Y, control the capacitance of the element and the amount of radiated power by the element. Similar to that process of [6] we designed the element with two PIN diodes for symmetry but only one is needed. Although slight adjustments were made to X and Y the predominant design knobs used were that of a, b, and the reversed bias capacitance of the PIN diode. X was kept somewhere near $\lambda_g/5$ to $\lambda_g/6$ while Y had more variation. Parametric sweeps were then carried out while monitoring S_{21} and S_{11} to ensure weak resonances and minimum reflected power, respectively. The radiated power was also monitored to prevent large radiation from the element as well as proving that the coupled guided wave is not being reflected. Throughout the entirety of this design laid out in this Chapter; Rogers RO4003 was utilized as the dielectric substrate with a thickness of 1.52 mm and ϵ_r = 3.55.

As a next step, the originally designed element was shifted near the edge of the PEC walls SIW. Resulting in shifts of the resonant frequency as well as tangible reduction in the radiated power (and coupling to the SIW mode). To overcome this further full-wave numerical simulations were performed with parametric sweeps to yield a desired response and resonant frequency. Following the physical shift of the element near the edge, a study was conducted with an introduction of a DC bias line on the top layer. Three separate

approaches were studied where a very thin microstrip line was used to bring DC signal at the side of the element. To implement this DC bias line, a small cut was made in the PEC walls as well as the top plate of the SIW (to separate their DC). All three cases of this study incorporate a radial decoupling stub to prevent power loss from the unintended radiated power coupling to the DC bias. The three DC bias approaches are shown in Figure 3.2, Figure 3.3, and Figure 3.4. In Figure 3.2 we brought the DC bias in at the center of the cELC resonator. The results of this investigation are shown in Figure 3.5. Extensively

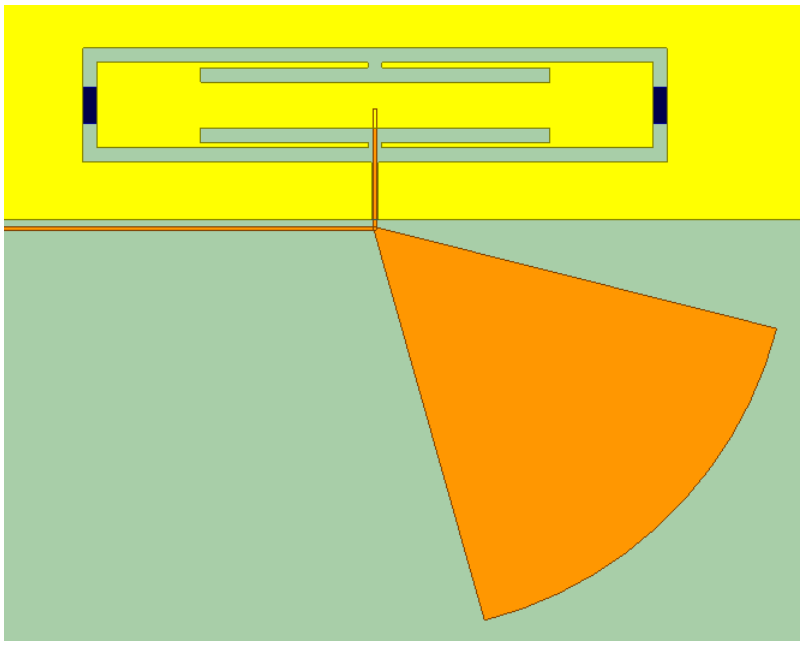

Figure 3.2: DC Bias Study - Center Bias

altering the physical dimensions of the element we were able to get a weak resonance seen in the S_{21} of all three cases. Although S_{11} is slightly improved it is equivalent to that of the other two feeds in this investigation. The frequency at which this bias was resonant is out of the desired range of 5.5-6.5 GHz and was dismissed as an option. Following the center bias approach, we attempted to bring the DC bias in at the top of the element edge as seen in Figure 3.3. This resulted in a stronger resonance at a lower frequency within the desired bandwidth seen in the results plot of S_{21}. The reflected power in S_{11} was comparable to the

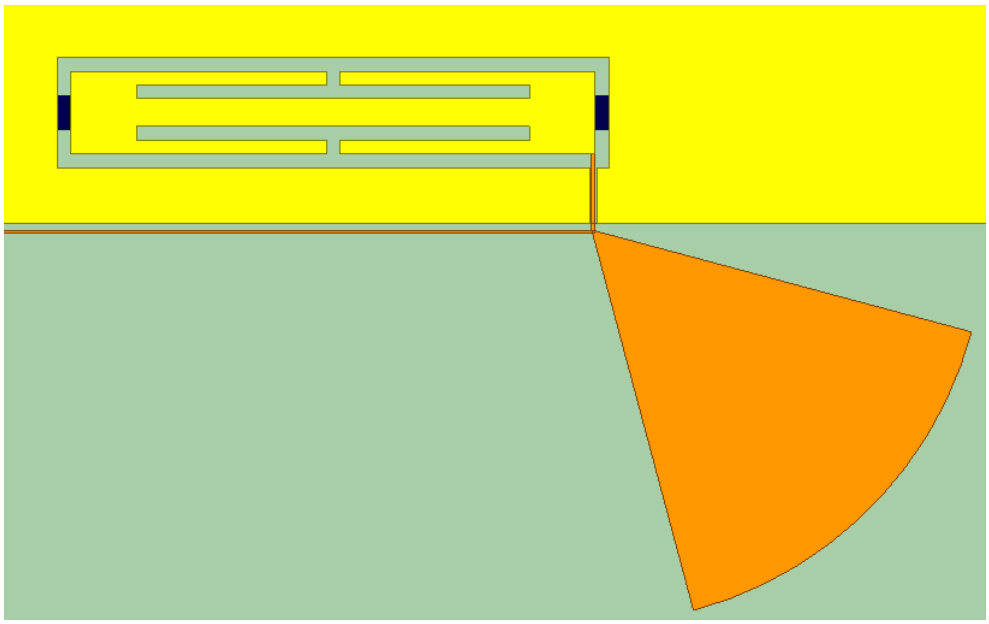

Figure 3.3: DC Bias Study - Edge Bias

other three designs. Finally, we arrived at the design where the bias is attached at the edge offset from the center by the protruding section of the cELC; a physical attribute of *b* as seen in Figure 3.4. This bias approach rendered a better resonance at the center frequency with increased radiated power than that of the top edge case. Operating off-center of the resonant frequency would also allow for a larger bandwidth than that of the top edge bias. Although the bias for this study changed locations the radial stub dimensions were kept constant with a length of 5.7 mm and etched at the same distance from the PEC wall of the SIW. Keeping the radial stub close to the walls of the SIW restricted coupling while reducing the antenna's size. Similar to the approach of [6], we terminated the DC bias as a lumped port allowing us to monitor S_{31} for leakage. The offset edge bias of this investigation rendered the best performance and is carried out for the remainder of this design moving forward. To investigate the benefits of the decoupling radial stub the offset edge bias approach was evaluated with and without the radial stub the results are shown in Figure 3.6. Although there is roughly a 10 dB improvement of isolation at the low end as well as the resonant frequency; the resonance is no longer present without the stub. This is

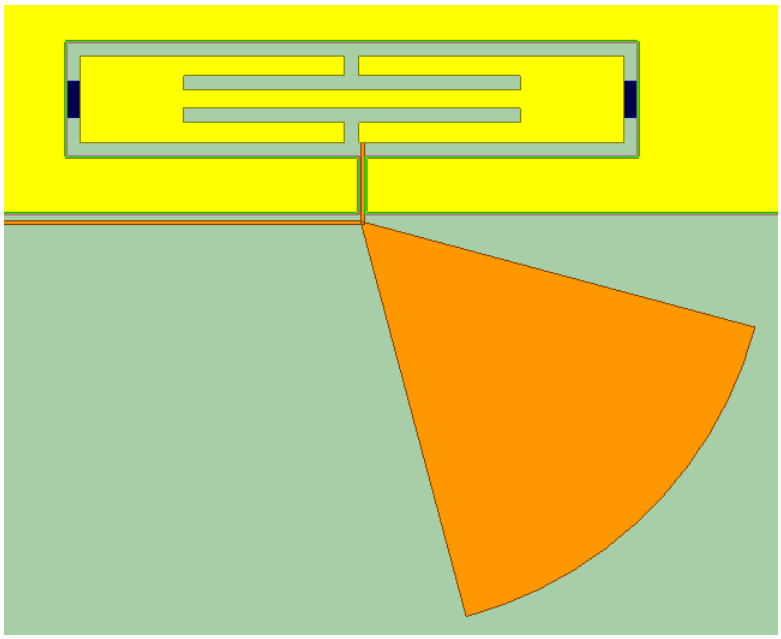

Figure 3.4: DC Bias Study - Offset Edge Bias

partially due to the change in complex impedance of the cELC resonator with the addition of the radial stub like that of [6]. The difference in this case is there was not a small shift in resonance but, an absolute loss of a resonant frequency within the bandwidth of interest.

Now that we have a working cELC resonator element with the DC bias on the same layer, we design a simple SIW antenna operational at C-band to arrive at the best response and via spacing. Having the proper spacing and location of vias in our current design led to removing the PEC side walls. The next step in the construction of the DMA array is adding metamaterial elements as a copy of our original design. Placement of the added element to prevent phase lag and render constructive performance was placed at $\lambda_g/2$ on the opposite side of the SIW. Copying this element includes the DC biasing line and the radial decoupling stub. At this spacing, the elements will easily couple to arrive at constructive radiation patterns. With the addition of more elements to prevent unwanted coupling the width of the SIW structure was expanded to 15.9 mm and carried out for the remainder of this chapter henceforth. To confirm the added element does not result in a resonant fre-

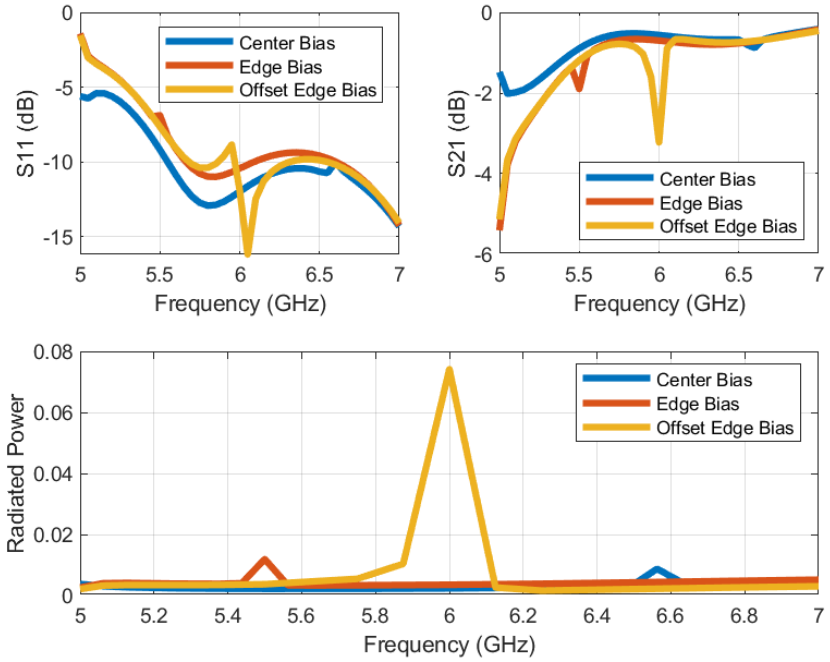

Figure 3.5: Investigation of DC Feed Location S-Parameters and Radiated Power

quency shift or any unforeseen degradation, we performed full-wave numerical simulations before adding more elements. In Figure 3.7 and Figure 3.8 it is shown that the second element actually helped reduce a slight steer to one side as a result of the spurious radiation from the connection of the DC bias line and the element. The element-pair geometry was then copied every λ_g. We evaluated the DMA for each addition of two elements and had a small shift in resonant frequency that was compensated by slightly changing the geometry of the element. It is worth emephasizng that we had to remove one or two vias to allow for addition of the DC bias lines. The final designed DMA is an 8-element array each with its own DC bias line and radial decoupling stub. Final design constraints for the element are X = 8 mm, Y = 1.2 mm, a = 0.25 mm, and b = 4.7 mm. To access the re-configurable nature of the PIN diodes C_{rev} = 0.2 pF, R_{rev} = 10 kΩ, C_{fwd} = 0 pF, and R_{fwd} = 2 Ω are used for the reversed and forward bias values.

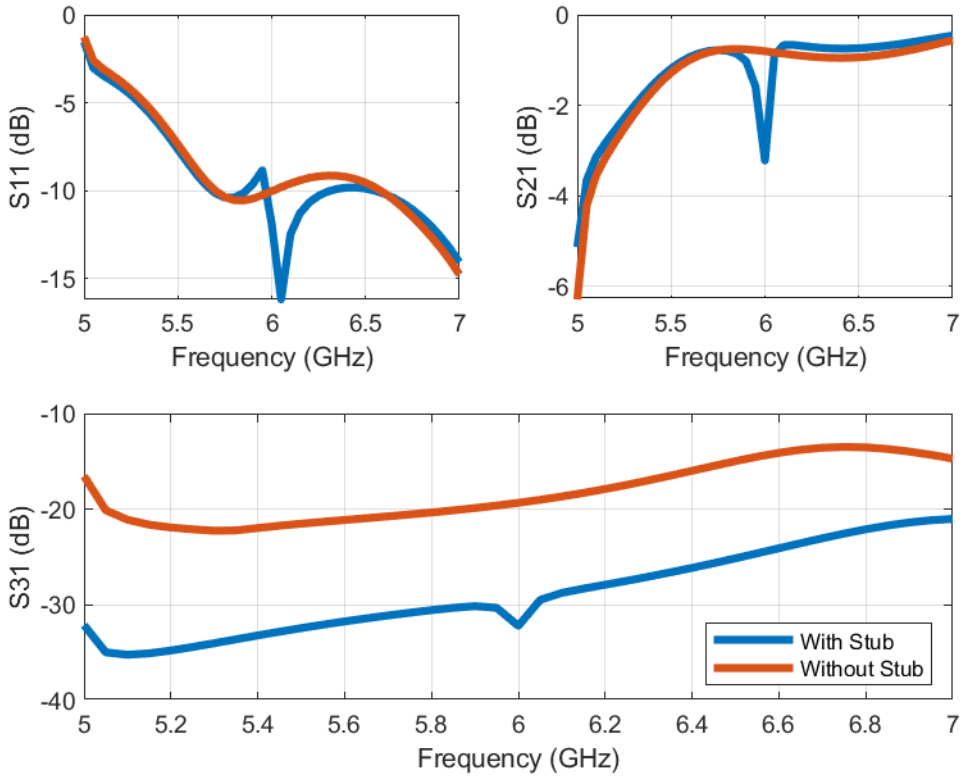

Figure 3.6: S-Parameters For Benefits of Radial Stub Investigation

3.3 Radiation Patterns for Array Element Using SIW

Since the final design of the 8-element array each has individually reconfigurable elements with separate DC bias lines, there is a total of 255 different element combinations, excluding the all-off case. Different combinations of elements, either being in forward or reversed bias, will be referred to as voltage masks henceforth. To limit the number of voltage masks to be simulated we randomly grouped two elements as one voltage mask group. This reduced the total number of unique voltage masks to 15. Thus making this simulation slightly easier while still being able to achieve various combinations of elements and unique patterns.

Full-wave numerical simulations were performed and a frequency sweep was conducted from 5.5 GHz to 6.5 GHz at 50 MHz steps for a total of 21 frequency points. For analysis

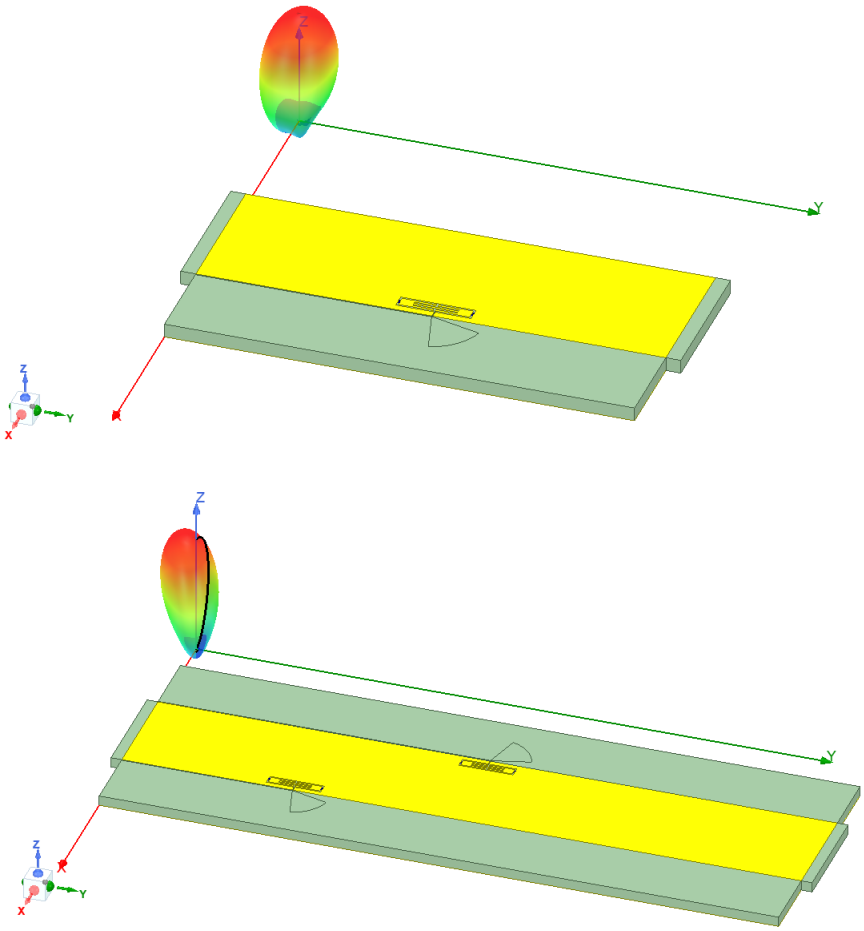

Figure 3.7: 3D View of Single Element versus Two Element Directivity Pattern Displayed on Antenna

of the DMAs potential for beamforming, the resonant frequency of the original metamaterial element on the initial SIW antenna is inspected along with complex beam patterns at various frequencies as well as various voltage masks. First, we look at the most directive beam at 5.65 GHz in Figure 3.10. Directive beams can be formed at various frequencies and even combinations of voltage masks with small side lobe levels.

Complex beams can be formed at various voltage masks for a single frequency of interest, shown in Figure 3.11. The uniqueness and complexity of these patterns are ideal for microwave imaging. The results shown in Figure 3.11 had each element individually addressable rather than the groupings of two previously discussed. We also reduced the

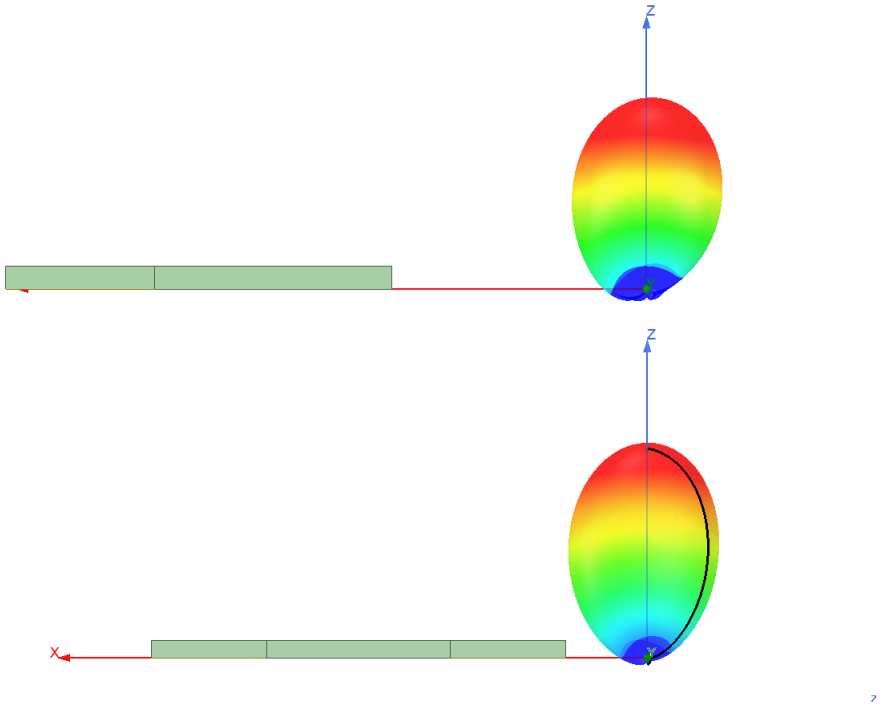

Figure 3.8: Direct View of Single Element versus Two Element Directivity Pattern Displayed on Antenna

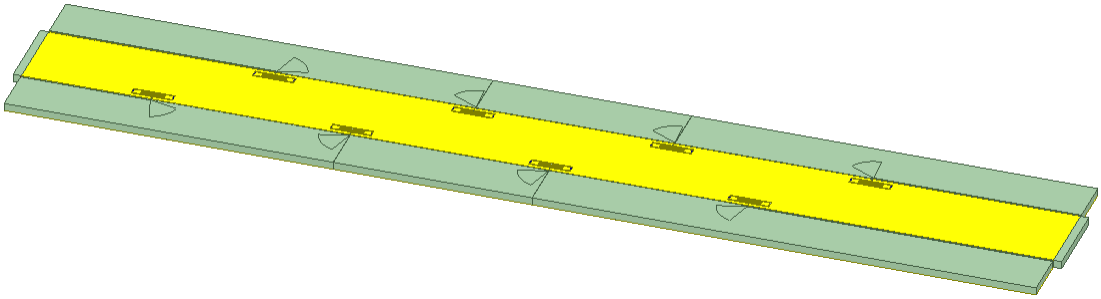

Figure 3.9: Top View of the Final DMA Array with Single Layer DC Feed and RF

element spacing to be $0.8\times\lambda_g/2$. The previous selection ensured constructive interference between elements near braodside. When the application is focused on forming complex patterns, smaller element spacing ensures different elements radiate with different phase. PIN diodes are low cost, making the overall cost and complexity of manufacturing inexpensive and simple, achieving the intended purpose of this design.

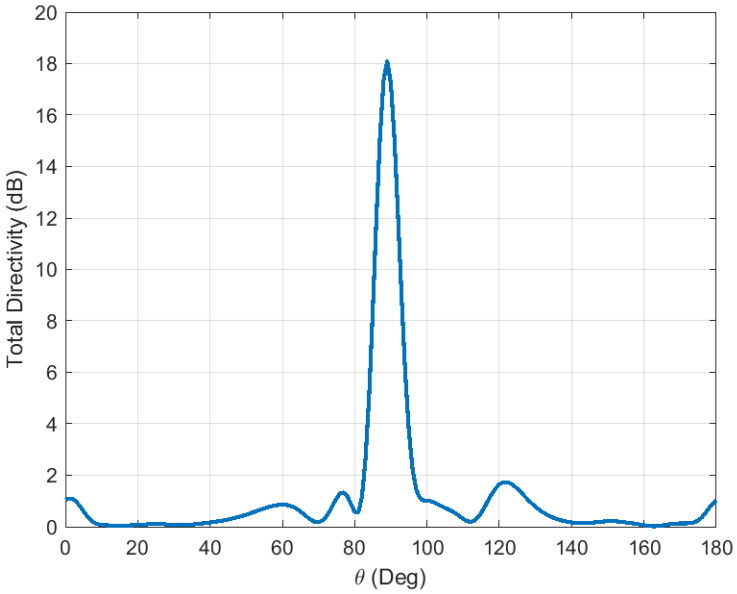

Figure 3.10: Maximum Total Directivity (dB) at 5.65 GHz

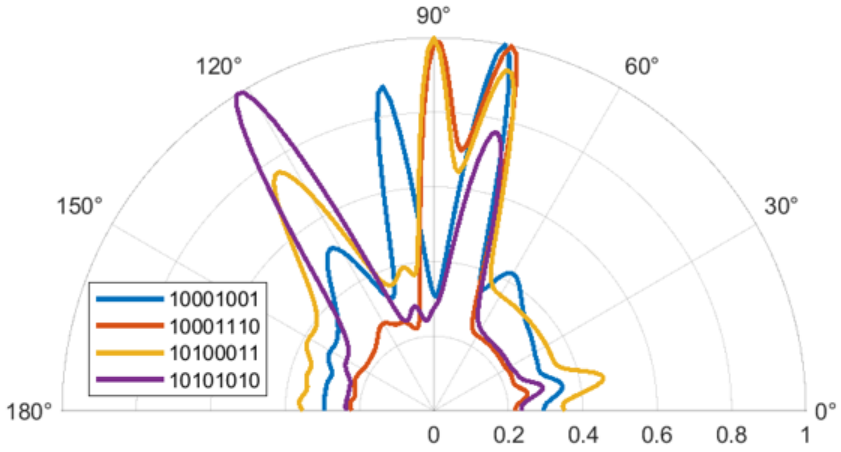

Figure 3.11: Normalized Directivity of Various Steered Beams

Chapter 4

CONCLUSION

4.1 Conclusion of Work

AoA detection was achieved for all reference angles through the *cgs* built-in solver in MATLAB. Investigation into both the minimum number of voltage masks to accomplish AoA detection as well as SNR additive noise for accurate estimations were investigated. The design of the planar DMA on a single layer for the radiating cELC resonant elements and DC circuitry in Chapter 3 was a success. Both directive and unique patterns were able to be formed and can be utilized for a number of applications. Designed as is the antenna could easily be adapted to a DCMA due to maintaining the simplicity of the single-layer approach. All while reducing the price and complexity to be manufactured in either a conformal or planar structure

4.2 Future Work

With the success of the single-layer DMA in Chapter 3 a few paths can be pursued in the future. One of which is building and measuring the antenna's performance compared to the simulated results. Ideally, the full simulated data set of 255 voltage masks would be used specifically to measure the unique patterns at various frequencies. Another potential study that could be conducted is forming the current array into a DCMA as is or multiple side-by-side carried out similarly to that of [19].

The more interesting path of study would be to take the single-layer designed element of Chapter 3 and implement the design into the structure of Chapter 2. Due to the single-layer design of the element, the DCMA structure is easily achievable. Fabrication of the

DCMA would be inexpensive and realizable diodes would be able to be purchased for the PIN diodes. Measurements could be conducted in a range to get highly accurate incident waves to impinge on the surface of the DCMA to build the $\mathbf{H}$ matrix. Different test angles could then be performed to track the accuracy of the antenna's AoA detection with the conjugate gradients squared method solver or least squares solver similar to that of [8]. To further expand on both the simulated and measured opportunities a deep neural network (DNN) or other machine learning models could be designed off $\mathbf{H}$ and supplied test angles to see how accurately it can predict AoA from the complex voltages.

REFERENCES

[1] D. R. Smith, J. B. Pendry, and M. C. Wiltshire, "Metamaterials and negative refractive index," *science*, vol. 305, no. 5685, pp. 788–792, 2004.

[2] C. Milias, R. B. Andersen, P. I. Lazaridis, Z. D. Zaharis, B. Muhammad, J. T. Kristensen, A. Mihovska, and D. D. Hermansen, "Metamaterial-inspired antennas: A review of the state of the art and future design challenges," *IEEE Access*, vol. 9, pp. 89 846–89 865, 2021.

[3] Y. Dong and T. Itoh, "Metamaterial-based antennas," *Proceedings of the IEEE*, vol. 100, no. 7, pp. 2271–2285, 2012.

[4] R. W. Ziolkowski and A. Erentok, "Metamaterial-based efficient electrically small antennas," *IEEE Transactions on antennas and propagation*, vol. 54, no. 7, pp. 2113–2130, 2006.

[5] C. L. Holloway, E. F. Kuester, J. A. Gordon, J. O'Hara, J. Booth, and D. R. Smith, "An overview of the theory and applications of metasurfaces: The two-dimensional equivalents of metamaterials," *IEEE Antennas and Propagation Magazine*, vol. 54, no. 2, pp. 10–35, 2012.

[6] T. Sleasman, M. F. Imani, W. Xu, J. Hunt, T. Driscoll, M. S. Reynolds, and D. R. Smith, "Waveguide-fed tunable metamaterial element for dynamic apertures," *IEEE Antennas and Wireless Propagation Letters*, vol. 15, pp. 606–609, 2016.

[7] T. Sleasman, M. F. Imani, J. N. Gollub, and D. R. Smith, "Dynamic metamaterial aperture for microwave imaging," *Applied Physics Letters*, vol. 107, no. 20, p. 204104, 11 2015. [Online]. Available: https://doi.org/10.1063/1.4935941

[8] M. F. Imani and I. Alamzadeh, "Conformal frequency-diverse metasurface for computational aoa detection," *IEEE Antennas and Wireless Propagation Letters*, vol. 22, no. 11, pp. 2634–2638, 2023.

[9] J. Hunt, T. Driscoll, A. Mrozack, G. Lipworth, M. Reynolds, D. Brady, and D. R. Smith, "Metamaterial apertures for computational imaging," *Science*, vol. 339, no. 6117, pp. 310–313, 2013.

[10] J. Gollub, M. F. Imani *et al.*, "Large metasurface aperture for millimeter wave computational imaging at the human-scale," *Scientific reports*, vol. 7, no. 1, p. 42650, 2017.

[11] J. Hunt, J. Gollub, T. Driscoll, G. Lipworth, A. Mrozack, M. S. Reynolds, D. J. Brady, and D. R. Smith, "Metamaterial microwave holographic imaging system," *JOSA A*, vol. 31, no. 10, pp. 2109–2119, 2014.

[12] G. Lipworth, A. Mrozack, J. Hunt, D. L. Marks, T. Driscoll, D. Brady, and D. R. Smith, "Metamaterial apertures for coherent computational imaging on the physical layer," *JOSA A*, vol. 30, no. 8, pp. 1603–1612, 2013.

[13] O. Yurduseven, M. A. B. Abbasi, T. Fromenteze, and V. Fusco, "Frequency-diverse computational direction of arrival estimation technique," *Scientific reports*, vol. 9, no. 1, p. 16704, 2019.

[14] T. Sleasman, M. F. Imani, A. V. Diebold, M. Boyarsky, K. P. Trofatter, and D. R. Smith, "Computational imaging with dynamic metasurfaces: A recipe for simple and low-cost microwave imaging," *IEEE Antennas and Propagation Magazine*, vol. 64, no. 4, pp. 123–134, 2022.

[15] M. Boyarsky, T. Sleasman, M. F. Imani, J. N. Gollub, and D. R. Smith, "Electronically steered metasurface antenna," *Scientific Reports*, vol. 11, pp. 4693–4703, 2021.

[16] T. Sleasman, M. Boyarsky, M. F. Imani, T. Fromenteze, J. N. Gollub, and D. R. Smith, "Single-frequency microwave imaging with dynamic metasurface apertures," *JOSA B*, vol. 34, no. 8, pp. 1713–1726, 2017.

[17] M. Falchi, D. Brizi, and A. Monorchio, "A preliminary study of a conformal electromagnetic metasurface for brain tumor detection," in *2023 17th European Conference on Antennas and Propagation (EuCAP)*, 2023, pp. 1–4.

[18] M. R. Hashemi and T. Itoh, "Electronically controlled metamaterial-based leaky-wave transmission-line for conformal surface applications," in *2009 IEEE MTT-S International Microwave Symposium Digest*, 2009, pp. 69–72.

[19] I. Yoo and D. R. Smith, "Pattern synthesis of conformal rectangular waveguide-fed metasurface antennas," in *2022 IEEE 22nd Annual Wireless and Microwave Technology Conference (WAMICON)*, 2022, pp. 1–4.

[20] Y. Wang, J. Su, Z. Li, Q. Guo, and J. Song, "A prismatic conformal metasurface for radar cross-sectional reduction," *IEEE Antennas and Wireless Propagation Letters*, vol. 19, no. 4, pp. 631–635, 2020.

[21] A. I. Semenikhin and D. V. Semenikhina, "Conformal prismatic cylindrical metasurfaces containing identical oam-modules for rcs reduction," in *2023 Radiation and Scattering of Electromagnetic Waves (RSEMW)*, 2023, pp. 300–303.

[22] T. Liu, L. Liu, H. Chen, H. Sun, Z. Jin, L. F. Chernogor, D. O. Batrakov, and Z. Sun, "A broadband circularly polarized antenna based on transparent conformal metasurface," *IEEE Antennas and Wireless Propagation Letters*, vol. 22, no. 12, pp. 3197–3201, 2023.

[23] J. Wang and R. Yang, "Generating high-purity directive circularly polarized beams from conformal anisotropic holographic metasurfaces," *IEEE Transactions on Antennas and Propagation*, vol. 70, no. 11, pp. 10 718–10 723, 2022.

[24] D. L. Marks, J. Gollub, and D. R. Smith, "Spatially resolving antenna arrays using frequency diversity," *JOSA A*, vol. 33, no. 5, pp. 899–912, 2016.